Principles of X-Ray Diffractometry of Surface Acoustic Waves

I. A. Schelokov

*Institute of Microelectronic Technology and High Purity Materials, Russian Academy of Sciences,
ul. Akademika Osip'yana 6, Chernogolovka, Moscow district, 142432 Russia*
e-mail: igor@iptm.ru
Received March 6, 2013

Abstract—Theoretical fundamentals of modern methods of X-ray diffractometry of surface acoustic waves (SAW) are considered briefly. X-ray diffraction on SAW-modulated crystals under total external reflection conditions and the Bragg conditions for the *YZ*-cut of the LiNbO$_3$ crystal is considered. Agreement of theoretical and experimental results makes it possible to use them for SAW diagnostics. Possibilities and limitations of listed methods for determining the SAW field parameters are discussed.

INTRODUCTION

Modern means of communication widely use acoustoelectronic devices based on surface acoustic waves (SAWs) in various telecommunication systems (mobile phones, pagers, radio, TV, etc.). The design of SAW devices is becoming increasingly more complex, which requires the development of new diagnostics methods of SAWs propagating in their acoustic tracts. High-resolution X-ray diffractometry with the use of synchrotron radiation sources is the most promising tool for diagnostics of acoustoelectronic devices and materials [1–4].

We performed excitation of the Rayleigh-type SAWs using the so-called interdigital transducer (IDT). It is a system of two ridged electrodes formed using lithography on the crystal surface, onto which a high-frequency (HF) signal is supplied. The structure of the SAW field, which is emitted by the IDT, is determined by many parameters, the most important of which is the shape of electrodes. Figure 1 schematically depicts the IDT with the arbitrarily varying shape of separate pins. Most often, the IDT with the same degree of overlap of pins, which are separated equidistantly, is used. If d is the distance between the teeth, then the IDT resonant excitation frequency and the SAW wavelength are determined by expression $f_0 = V/2d$ and $\Lambda = V/f_0$, respectively. Here, V is the velocity of sound, which equals 3488 m/s for the *YZ* cut of the LiNbO$_3$ crystal.

SAW diagnostics is performed using various methods. Good results are given by visualization of the SAW fields on a screen of a scanning electron microscope (SEM diagnostics). In this case, the contrast of formed images is potential, i.e., it is proportional to the distribution of the piezoelectric potential. Therefore, using

an SEM, we can determine the SAW wavelength and velocity but not its amplitude [5].

SAW diagnostics with the use of the laser technique are most widespread presently. They are not considered in this article. Let us note only the following circumstance: working frequencies of modern acoustoelectronic devices continuously increase and currently constitute 0.9–2.5 GHz. This means that the SAW wavelength becomes an order of several microns at the amplitude of several angstroms. The laser radiation wavelength is larger than 3000 Å. The attainment of resolution of $\lambda/1000$ is at least a very laborious problem not even mentioning the possible error of such measurements. Laser SAW diagnostics should be substituted by other methods, such as the above-mentioned SEM diagnostics or the diagnostics using the X-ray radiation with a wavelength of an order of angstroms. These methods or, more correctly, their physical foundations, will be discussed below.
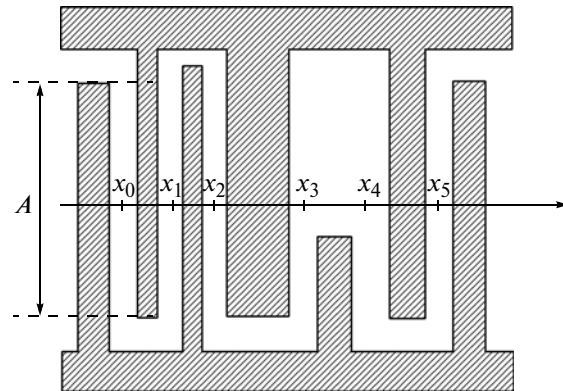

Fig. 1. IDT with arbitrarily varying shape of separate tips.

DIFFRACTION OF X-RAY RADIATION ON THE SAW IN CONDITIONS OF TOTAL EXTERNAL REFLECTION (TER)

Refraction index n for all substances in the X-ray wavelength range is much smaller than unity:

$$n = 1 - \delta + i\beta.$$

Depending on the radiation wavelength, this difference is from 10^{-2} to 10^{-11}. From the viewpoint of optics, this means that a vacuum is the medium optically denser compared with the substance (Fig. 2). According to this fact, by analogy with the total internal reflection effect in optics of the visible wavelength range, the total external reflection (TER) effect is observed for X-ray radiation.

In the X-ray wavelength range, the incidence angle is counted from the surface rather than from the normal to it. It is sometimes called the grazing, which is correct. However, the old name is used more often. Since X-ray radiation penetrates inside the crystal under study in TER conditions only insignificantly, diffraction can be described correctly in the framework of rather simple model [6]. Its main statements are as follows.

Taking into account that radiation reflectances in TER conditions for various polarization directions are identical, the diffraction pattern can be calculated in terms of the Kirchhoff scalar diffraction theory:

$$u(P) = \frac{1}{4\pi} \iint\limits_{S} \left(G\frac{\partial u}{\partial \mathbf{n}} - u\frac{\partial G}{\partial \mathbf{n}} \right) dS, \quad (1)$$

where $u(P)$ is the field amplitude in point P; $G = \exp(ikr)/r$ is the Green's function for free space; $d/d\mathbf{n}$ denotes the derivative with respect to the direction of the outer normal to the surface; S is the closed surface, including the crystal surface and the infinitely remote hemisphere above it; and dS is the surface element.

The interaction between X-ray radiation and the substrate is described based on the Fresnel formulas for the interface between two media. We assume that the Fresnel formulas are valid locally in each point of the surface, which is formed by the SAW relief. It should be taken into account that, because of the smallness of the distinction of the refractive index from unity, the critical angle in the X-ray wavelength range is also very small:

$$\theta_c = \sqrt{\delta/2}.$$

For example, at $\lambda = 1.54$ Å (CuK_α), $\theta_c \approx 0.56°$ even for so dense a substance as tungsten. Therefore, even if the angles formed by the profile of the SAW relief with the unperturbed crystal surface are very small, the situation is possible when the radiation incidence angle
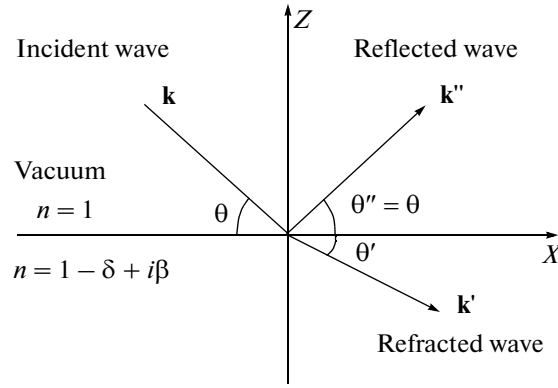

Fig. 2. Path of rays at the interface in the X-ray diffraction wavelength range.

for a part of the SAW period already exceeds the critical angle. For the reflectance, we have

$$R = R(\alpha + \varphi) = R(\alpha + \arctan(hK\cos Kx)), \quad (2)$$

where it is accepted that function $h\sin Kx$ describes the profile of the SAW relief, h is the SAW amplitude, $K = 2\pi/\Lambda$ is the modulus of the SAW wave vector, α is the radiation incidence angle, and $\varphi = \arctan(hK\cos Kx)$ describes the angle of misorientation because of the SAW relief.

For the same reason, we should take into account the orientation of the elementary surface area relative to the wave vector of the incident wave. This means that the integration is performed over the "corrugated" surface—the SAW relief. Allowing for this fact, expressions for the normal and the elementary area have the form

$$dS = \frac{dx\,dy}{n_z},$$

$$n_x = \frac{hK\cos Kx}{\sqrt{1 + (hK\cos Kx)^2}}, \quad (3)$$

$$n_z = \frac{-1}{\sqrt{1 + (hK\cos Kx)^2}}.$$

The above-described model is in many respects similar to that one used in visible range optics, i.e., in laser diagnostics methods. The last two items of this model are usually neglected since the radiation incidence angles are rather large. The influence of the SAW relief is taken into account only when calculating the phase incursion. However, for the laser diagnostics, the model is nevertheless complicated since we should take into account the crystal anisotropy with respect to the radiation reflection from the sample surface. Figure 3 represents the coordinate system for the calculation of diffraction of the plane incident wave.
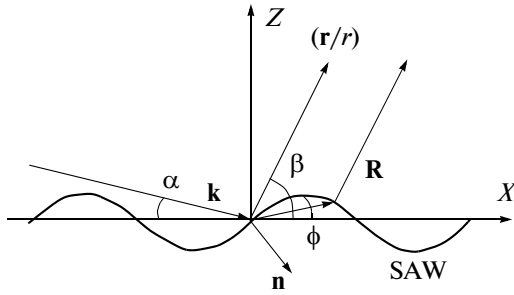
Fig. 3. Coordinate system for the calculation of diffraction of the plane incident wave on the SAW.

Fig. 4. To the calculation of the phase shift in the field of incident plane wave on the crystal surface with the SAW.

Taking into account the aforesaid, under the condition that quasi-plane wave $u(\mathbf{r}) = u_0(\mathbf{r})\exp(i\mathbf{k}\mathbf{r})$ falls on the surface, i.e., $\partial u_0/\partial \mathbf{r} = 0$, we derive:

$$\frac{\partial u}{\partial \mathbf{n}} = i(\mathbf{k}\mathbf{n})u,$$

$$\frac{\partial}{\partial \mathbf{n}}\left(\frac{\exp(ikr)}{r}\right) = \left(ik - \frac{1}{r}\right)\frac{\exp(ikr)}{r}\left(\frac{\mathbf{r}}{r}\mathbf{n}\right), \quad (4)$$

where $\mathbf{k} = (k\cos\alpha, 0, -k\sin\alpha)$ is the wave vector of the incident wave and $\mathbf{n} = (n_x, 0, n_z)$ is the normal to the SAW surface. The substitution of expression (4) into (1) allowing for $kr \gg 1$ leads to the expression:

$$u(P) = \frac{i}{4\pi}\iint_S u\frac{\exp(ikr)}{r}\left(\left(\mathbf{k} - k\frac{\mathbf{r}}{r}\right)\mathbf{n}\right)dS,$$

or, if we open the scalar product,

$$u(P) = \frac{k}{4\pi i}\iint_S u\frac{\exp(ikr)}{r}$$
$$\times (n_z(\sin\alpha + \sin\beta) - n_x(\cos\beta - \cos\alpha))dS. \quad (5)$$

We can notice that if $\mathbf{n} = (\sin\varphi, 0, -\cos\varphi)$, where φ is the angle formed by the SAW profile with axis X, then the angular multiplier takes its standard form:

$$-\sin(\alpha + \varphi) - \sin(\beta - \varphi) = \cos(\mathbf{n}\mathbf{r}) - \cos(\mathbf{n}\mathbf{k}).$$

Let us now calculate the phase shift on the SAW surface caused by the path difference in the incident wave (Fig. 4). Path difference Δ is the magnitude of the AB segment. With no allowance for the surface relief height, the path difference is $\Delta = x\cos\alpha$. Allowing for the surface relief height, the path difference in the incident wave is:

$$\Delta = CB\sin\alpha,$$

$$CB = CD - BD = \frac{x}{\tan\alpha} - z,$$

$$\Delta = \left(\frac{x}{\tan\alpha} - z\right)\sin\alpha = x\cos\alpha - z\sin\alpha,$$
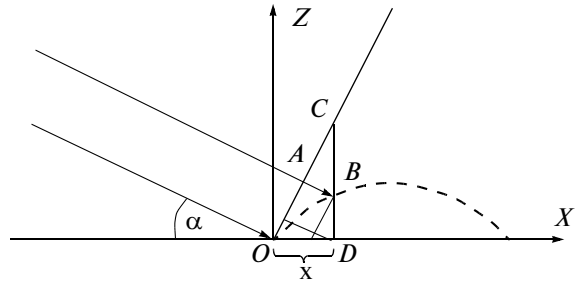
$$z = h\sin Kx.$$

It is seen that, at $z \to 0$, the path difference in the incident plane wave $\Delta \to x\cos\alpha$, which was found previously. Thus, the incident plane X-ray wave produce the field distribution on the SAW surface

$$u = u_0\exp(ik(x\cos\alpha - z\sin\alpha)).$$

Considering similarly the contribution of surface element dS with radius-vector $\mathbf{R}$ in point P into the amplitude of the reflected wave in far zone, we can notice that it has the additional phase multiplier

$$\exp(ik(-x\cos\beta - z\sin\beta)),$$

relative to the corresponding contribution from point O, which corresponds to the origin of coordinates.

In addition, we should take into account that the amplitude of the contribution of each surface element will be proportional to the local reflectance (expression (2)).

Let us substitute all expressions into (5) and, taking into account that the integrand is independent of coordinate y and integration over it gives constant, we derive:

$$u(P) = \mathrm{const}\frac{\exp(ikr)}{\sqrt{r}}\int_{-N\Lambda/2}^{N\Lambda/2}\exp(ik[x(\cos\alpha - \cos\beta)$$
$$- h\sin(Kx)(\sin\alpha + \sin\beta)])\{(\sin\alpha + \sin\beta)$$
$$+ hK\cos(Kx)(\cos\alpha - \cos\beta)\}$$
$$\times R(\alpha + \arctan(hK\cos(Kx)))dx, \quad (6)$$

where Λ is the SAW wavelength and N is the number of periods illuminated by the incident plane X-ray wave. Using the known identity for the Bessel functions

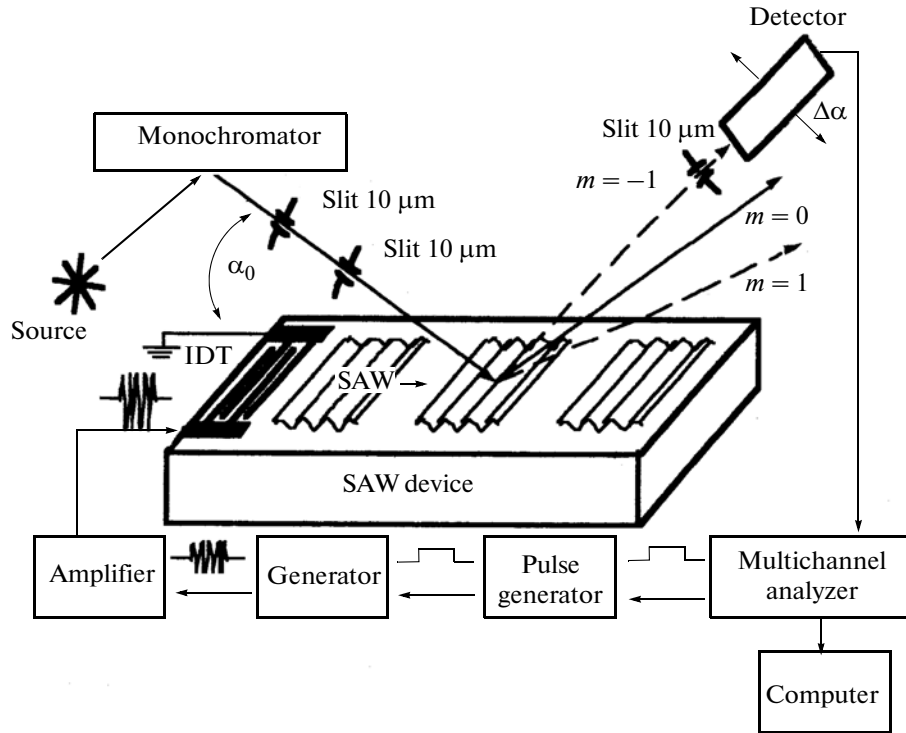$$\exp(i\xi\sin\beta\varphi) = \sum_{m=-\infty}^{\infty}J_m(\xi)\exp(im\varphi),$$

Fig. 5. Block diagram of the experiment with the use of the double-crystal X-ray diffractometer.

where $J_m(\xi)$ is the m-order Bessel function, we can easily simplify expression (6):

$$u(P) = \text{const}\frac{\exp(ikr)}{\sqrt{r}}$$

$$\times \int_{-N\Lambda/2}^{N\Lambda/2} R(\alpha + \arctan(hK\cos(Kx)))$$

$$\times \sum_{m=-\infty}^{\infty} J(kh(\sin\alpha + \sin\beta))$$

$$\times \exp(i[k(\cos\alpha - \cos\beta) - mK]x)$$

$$\times \{(\sin\alpha + \sin\beta) + hK\cos(Kx)(\cos\alpha - \cos\beta)\}dx.$$

From the viewpoint of the SAW diagnostics, it is desired that all segments of the modulated surface would be in TER conditions. This is implemented experimentally rather simply. In this case, the reflectance on the SAW relief is almost invariable, and, under the assumption of its constancy and smallness of the second summand in the angular multiplier, the expression is easily integrable and takes the form:

$$u(P) = \text{const}\frac{\exp(ikr)}{\sqrt{r}}2\pi R_{\text{const}}$$

$$\times \sum_{m=-\infty}^{\infty} J(kh(\sin\alpha + \sin\beta))$$

$$\times \delta(k(\cos\alpha - \cos\beta) - mK)(\sin\alpha + \sin\beta).$$

Thus, the solution represents a divergent cylindrical wave with a complex angular dependence. It follows from the practical experience of using this formula that the best results can be obtained if not peak values of intensity of diffraction satellites but their integral intensity are taken as the experimental values.

We considered the diffraction process for the case of a plane wave in TER conditions since it is simpler mathematically and clearer physically. In final computations of the diffraction pattern, we additionally took into account the beam divergence, i.e., each point of the source emits a spherical wave [6].

Experimental measurements were performed in a standard layout of a double crystal X-ray diffractometer (Fig. 5) [6]. The radiation from a source with a rotating copper anode (CuK_α radiation, $\lambda = 1.54$ Å) after a monochromator crystal was collimated by a system of two slits 10 μm wide each. The studied sample was YZ cut of the LiNbO$_3$ crystal. The IDT with electrodes 8 μm wide, which corresponds to the SAW wavelength of 32 μm, was formed on the crystal surface so that the SAW would propagate in the Z axis direction with velocity $V = 3.488$ km/s. A resonant excitation frequency of the IDT was $f_0 = 109$ MHz with transmission band $\Delta f/f_0 = 12.8\%$ ($f = 100-114$ MHz). The experimentally measured critical angle for LiNbO$_3$ was $\theta_c = 0.30°$. The comparison of calculated and experimental data is presented in Figs. 6 and 7.

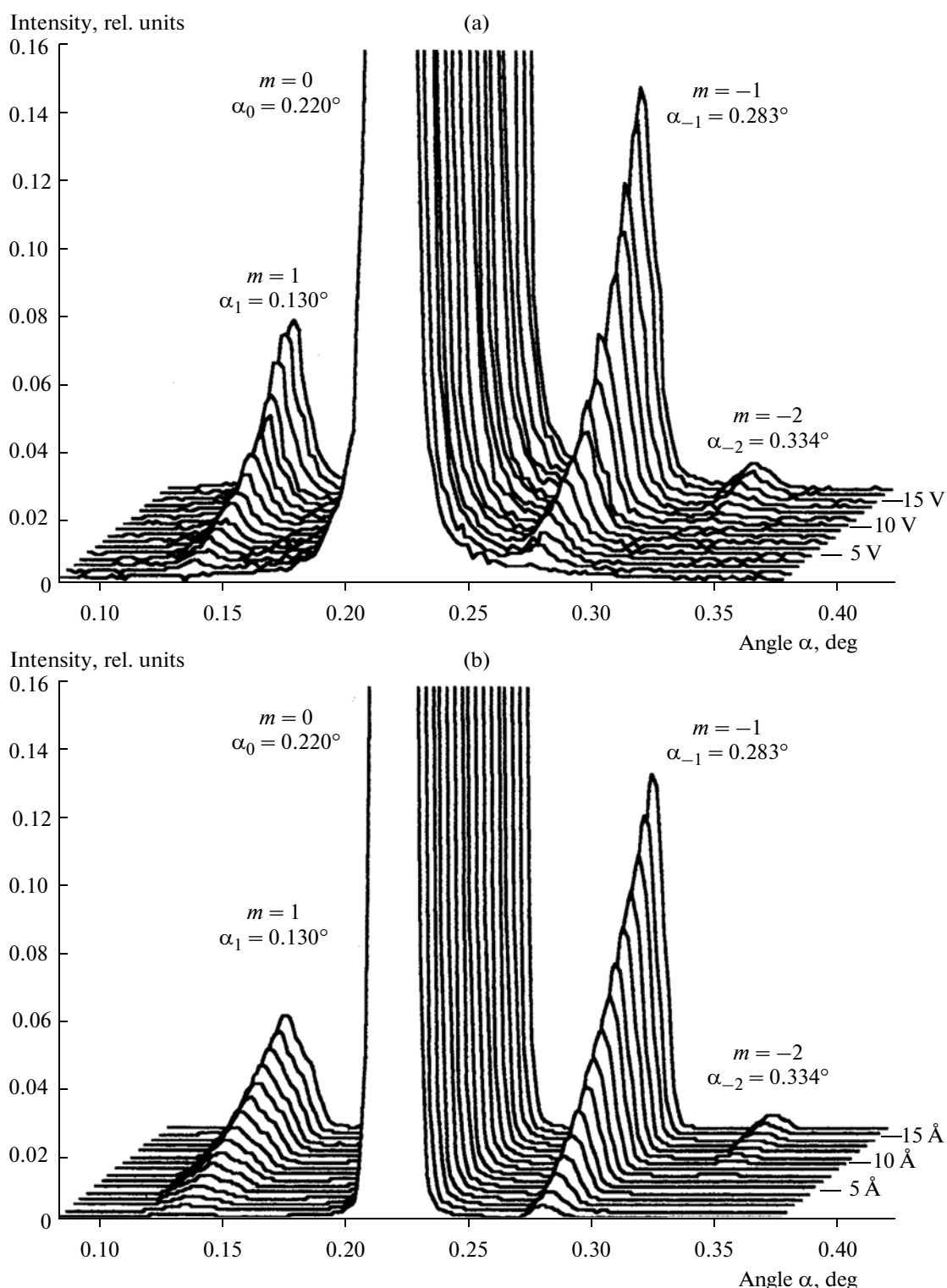Despite the found good correspondence, this method possesses some substantial limitations,

Fig. 6. Comparison of (a) experimental and (b) calculated diffraction curves depending on the voltage across the IDT and the SAW amplitude, respectively ($h/U = 1$ Å/V).

which do not make it suitable for practical application. First, these are the requirements to the surface quality—the crystal surface should be polished to atomic smoothness, otherwise an abrupt increase in the diffuse scattering on the rough surface will lead to large error in SAW amplitude diagnostics. It is clear that industrial samples are not subjected to such a treatment. Second, as was already noted, modern
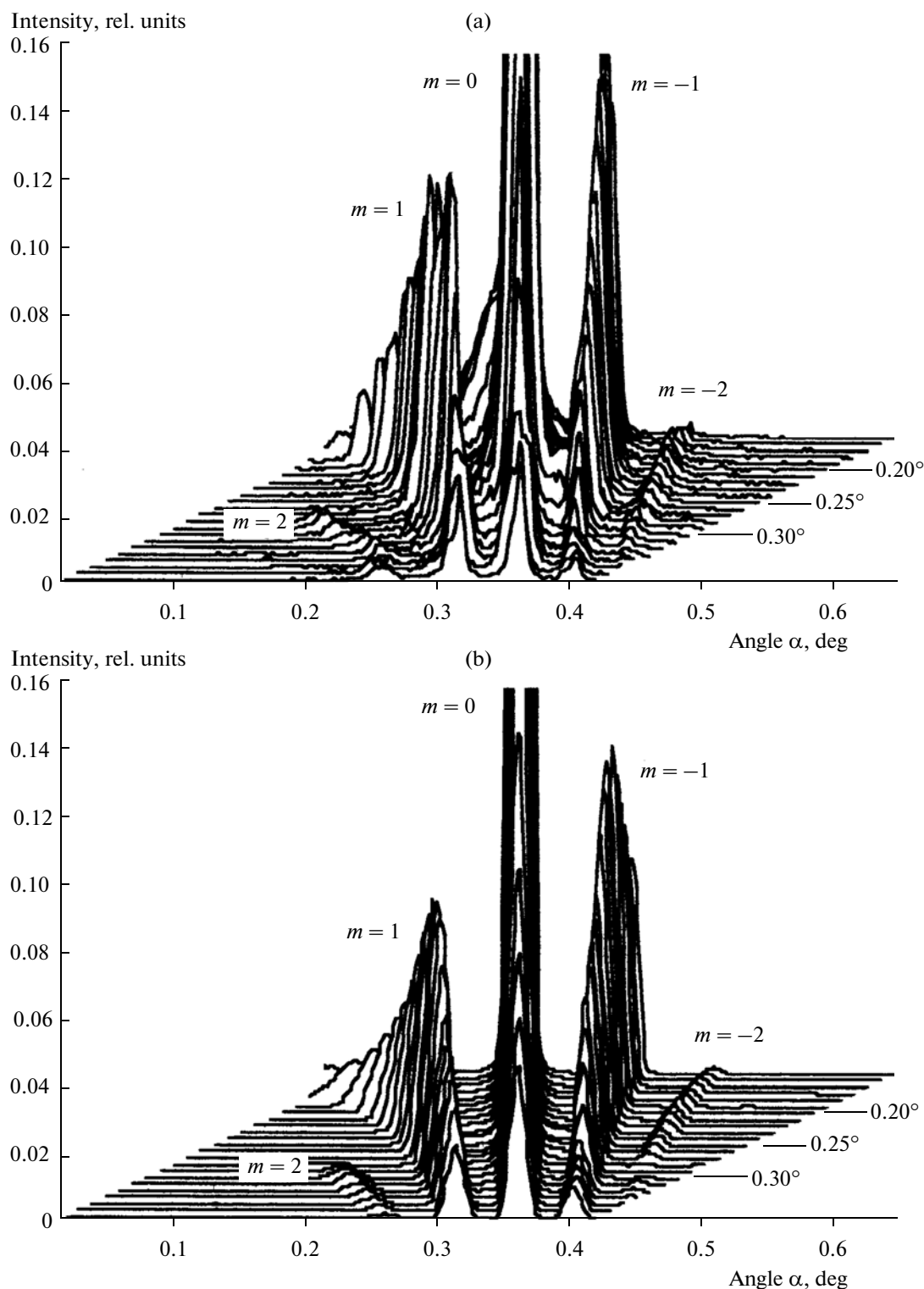
Fig. 7. Comparison of (a) experimental and (b) calculated diffraction curves depending on radiation incidence angle $\alpha = 0.15-0.37°$ ($U = 17$ V).

SAW devices operate at microwave frequencies (up to 3 GHz) with the excited wavelength of the order of several microns. The divergence of diffraction orders increases in this case and it turns out that the diffrac- tion angle of satellites becomes larger than that criti- cal for this X-ray radiation wavelength. The method based on the use of the Bragg diffraction is free of these limitations.
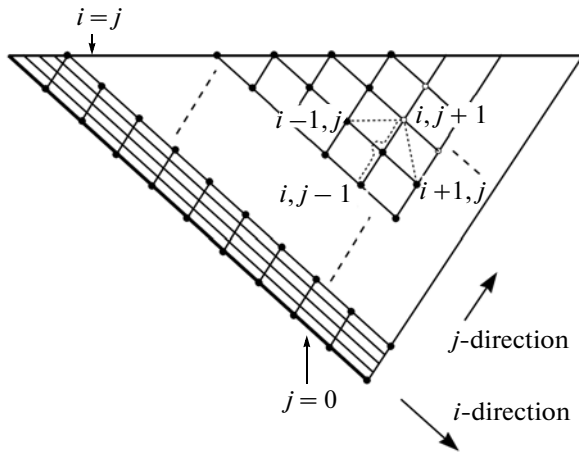
Fig. 8. Mesh for the numerical integration of the Takagi–Taupin equations.

BRAGG DIFFRACTION ON THE PIEZOELECTRIC CRYSTAL WITH SAWS

Let us solve the problem of X-ray radiation diffraction in a piezoelectric crystal with SAWs for the *YZ* cut of the LiNbO$_3$ crystal. This solution involves the calculation of the deformation of the crystal lattice caused by the Rayleigh-type surface wave and simulation of wave fields in the crystal based on the Takagi–Taupin equations. We restrict ourselves only by the statement of problems in the theoretical part of the section.

The dynamic theory of X-ray radiation diffraction in deformed crystals was developed in works of many authors [7−9]. For the SAW-modulated crystals, we will consider that atomic planes are only shifted relative to their positions in the ideal crystal without varying its scattering ability. Then, the polarizability of the deformed crystal $\chi(\mathbf{r})$ can be represented in the form:

$$\chi(\mathbf{r}) = \chi^{id}(\mathbf{r} - \mathbf{u}(\mathbf{r})) = \sum_{g.} \chi_g^{id} \exp(i\mathbf{g}(\mathbf{r} - \mathbf{u}(\mathbf{r}))) \quad (7)$$

Polarizability $\chi(\mathbf{r})$ of the ideal crystal is a three-dimensional periodic function and, consequently, it can be expanded into the Fourier series over vectors of a reciprocal lattice $\mathbf{g}$. This is valid under the fulfillment of the condition

$$\left| \frac{\partial u_i}{\partial x_k} \right| \ll 1,$$

which is almost always fulfilled for the propagation of elastic waves in crystals. Here, $\mathbf{u}(\mathbf{r})$ is the function specifying the SAW deformation field (the function that describes the shifts of atoms relative to their positions in the ideal crystal).

With allowance for this fact, the final set of equations for slowly varying field amplitudes (the Takagi–

Taupin equations) for X-ray radiation diffraction with the deformation field introduced by SAWs can be written as

$$\begin{cases} -2i(\mathbf{k}_0 \nabla)\mathbf{D}^0 = \chi_0^{id}\mathbf{D}^0 + C\chi_{-g}^{id}\mathbf{D}^g \exp(i\mathbf{g}\mathbf{u}(\mathbf{r})) \\ -2i(\mathbf{k}_g \nabla)\mathbf{D}^g = C\chi_g^{id}\mathbf{D}^0 \exp(-i\mathbf{g}\mathbf{u}(\mathbf{r})) + (\chi_0^{id} - \alpha)\mathbf{D}^g. \end{cases} \quad (8)$$

The set of equations (8) admits the following interpretation: with the propagation inside the crystal, field $\mathbf{D}^0$ receives additional phase shift and exchanges energy with the field of diffracted wave $\mathbf{D}^g$. In addition, in each point $\mathbf{r}$ of the crystal, the diffracted (term $C\chi_g\mathbf{D}^0$) and twice-scattered field (term $C\chi_{-g}\mathbf{D}^g$) receive additional (compared with the ideal crystal) phase shifts $\exp(-i\mathbf{g}\mathbf{u}(\mathbf{r}))$ and $\exp(i\mathbf{g}\mathbf{u}(\mathbf{r}))$, respectively. This set of equations was used for the numerical calculation of propagation of wave fields in the crystal (Fig. 8).

The calculation of the SAW deformation field—function $\mathbf{u}(\mathbf{r})$, which enters this set of equations—is based on the approach described in [10, 11]. Here, we will represent only the problem statement and results of its solution.

Elastic waves in the piezoelectric anisotropic medium should satisfy the following set of equations:

$$\rho \frac{\partial^2 u_i}{\partial t^2} = c_{ijkl} \frac{\partial^2 u_i}{\partial x_j \partial x_k} + e_{kij} \frac{\partial^2 \Phi}{\partial x_j \partial x_k}, \quad (9)$$

where u_i are the components of displacement the particles in the elastic wave of our interest, c_{ijkl} is the tensor of elasticity moduli, e_{kij} is the tensor of piezoelectric moduli, ρ is the medium density, and $E_k = -\frac{\partial \Phi}{\partial x_k}$ is the quasi-static electric field associated with the wave. In addition, the electric induction of the piezoelectric field should satisfy the anisotropic Poisson equation for a nonconducting medium ($\text{div}\mathbf{D} = 0$):

$$e_{jkl} \frac{\partial^2 u_l}{\partial x_j \partial x_k} - \varepsilon_{jk} \frac{\partial^2 \Phi}{\partial x_j \partial x_k} = 0, \quad (10)$$

where ε_{jk} is the permittivity tensor.

This set of equations should be added by "mechanical" boundary conditions, which are involved in the equality to zero of mechanical stresses at free surface $x_2 = 0$ of the crystal (Fig. 9),

$$T_{i2} = c_{i2kl} \frac{\partial u_k}{\partial x_l} + e_{kl2} \frac{\partial \Phi}{\partial x_k} = 0, \quad i = 1, 2, 3, \quad (11)$$

and electrical boundary conditions, which should provide continuity of electric potential Φ and the electric induction normal component:

$$D_2 = e_{2kl} \frac{\partial u_k}{\partial x_l} - \varepsilon_{2l} \frac{\partial \Phi}{\partial x_i}. \quad (12)$$

Set of Eqs. (9) and (10) with boundary conditions (11) and (12) should be solved for a plane wave propa-
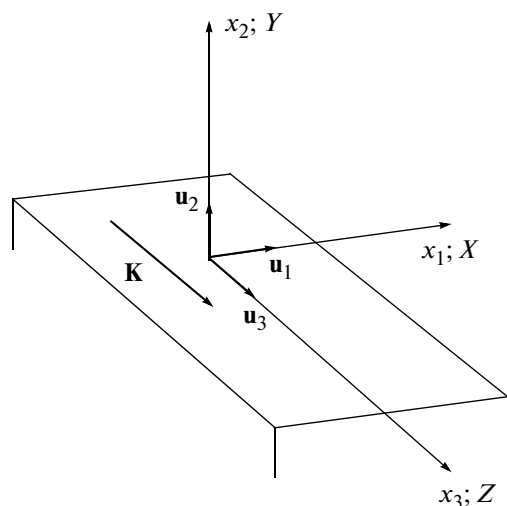
Fig. 9. Coordinate system for the calculation of shift components **u** in the surface acoustic wave propagating along the *YZ* cut of the lithium niobate crystal. **K** is the wave vector of the acoustic wave.

and the longitudinal component retards behind the transverse one over the phase by $\pi/2$. The size of the visualized deformation region of the crystal lattice along both axes is $2\Lambda_{ac}$. The term "schematically" was used since the SAW amplitude in reality is much lower than the ultrasound wavelength ($H \sim 1-10$ Å, $\Lambda_{ac} \sim 10$ μm). However, we could not represent the calculated deformation field in different scales over axes, since it would be impossible to see deformation damping into the crystal lattice depth (damping occurs at a depth of the order of units Λ_{ac}). Therefore, despite the fact that the exactly calculated field of SAW deformations is shown for the *YZ* cut of the lithium niobate crystal, we use the term "schematic" for it. Figure 10 makes it possible to represent clearly the features of the SAW deformation field, which are necessary to understand the further description.

If we imagine that horizontal lines in Fig. 10 correspond to atomic planes, we notice that the interplanar distance changes after the deformation (compared with the undeformed crystal lattice). This variation in the interplanar distance is especially noticeable on the slopes of the SAW profile, although this is a purely visual effect. In reality, this change is present everywhere so that the lithium niobate crystal is somewhat compressed in the SAW minima and stretched in the maxima. This is the main factor that should be emphasized. In addition, we can see the shift of the SAW
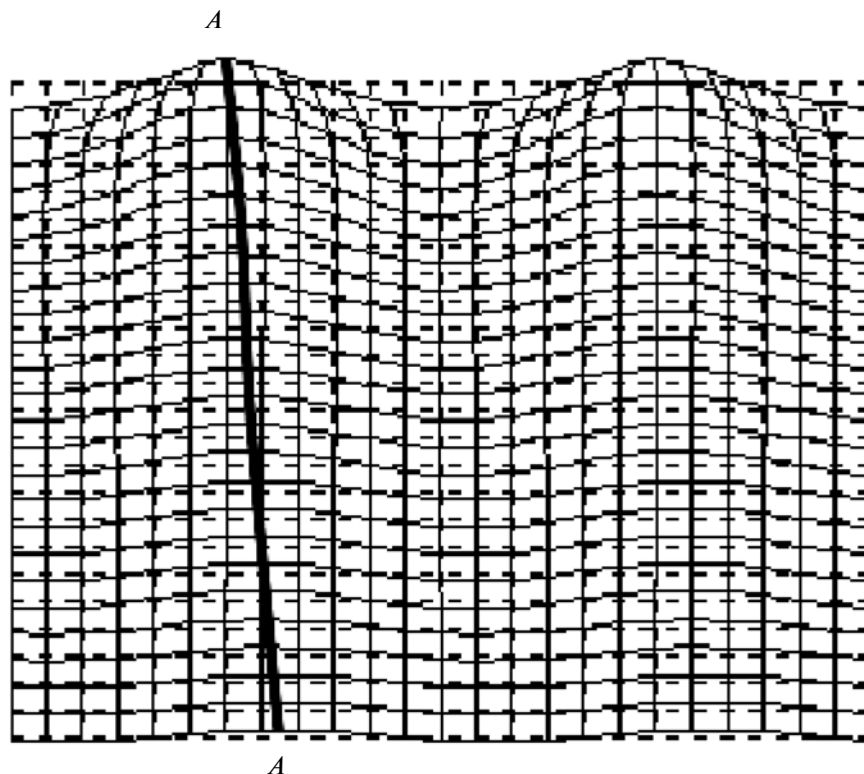
gating in the *Z* axis direction along the *YZ* cut of the lithium niobate crystal.

Our calculated SAW deformation field is schematically shown in Fig. 10. The longitudinal and transverse components of the shift are present in the SAW,

Fig. 10. Deformation of the crystal lattice caused by SAW propagation along the *YZ* cut of the LiNbO$_3$ crystal.
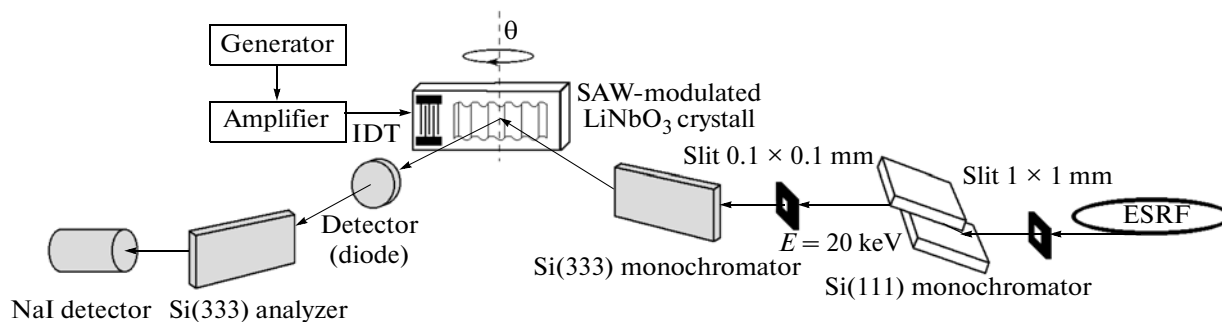
Fig. 11. Block diagram of the experiment with the use of a triple-crystal X-ray diffractometer.

maxima with deformation damping into the crystal depth. This shift is denoted by line *A* in Fig. 10.

Experimental investigations into X-ray radiation diffraction on the *YZ* cut of the SAW-modulated lithium niobate crystal were performed using an optical line (BM05) of the ESRF synchrotron radiation source [12]. Figure 11 represents a block diagram of a high-resolution triple-crystal diffractometer used to record X-ray spectra.

X-ray radiation with energy $E = 13$ keV after the Si(111) double monochromator crystal diffracts in a vertical plane. A slit 0.1×0.1 mm in size was used to collimate X-ray radiation. A second Si(333) monochromator crystal was established directly before the studied lithium niobate crystal in order to form a highly monochromatized X-ray beam ($\Delta\lambda/\lambda \sim 10^6$). To investigate the possibility of visualizing the diffraction satellites on the rocking curve after the LiNbO$_3$ crystal, a detector (photodiode) was established in the optical circuit. The Si(333) crystal was used as the analyzer crystal. To detect X-ray radiation after the analyzer crystal, the scintillation NaI detector was used.

To obtain the X-ray spectrum, the LiNbO$_3$ crystal rotated near the Bragg angle, which was equal to $\theta_{Br} = 18.715°$ in this case. We emphasize that we will discuss in this article only the spectra obtained in the double-crystal diffractometer circuit (without the analyzer crystal). In this case, the detector (photodiode) completely detected the radiation that emerged from the crystal under study since the detector window was opened completely. Thus, if the detector did not resolve spatial satellites in space, there was no necessity to solve the problem of radiation propagation in free space.

Figure 12 shows three rocking curves of the SAW-modulated LiNbO$_3$ crystal (*YZ* cut): one experimental curve (curve *1*) and two theoretical ones. The experimental curve is obtained at the amplitude of high-frequency electric signal across the IDT of 1.2 V. Curve *2* is calculated for a plane incident wave at ultrasound amplitude $H = 0.7431$ Å, which constitutes half-interpla-

nar spacing $d = 1.4862$ Å for reflection 030. Curve *3* is a rocking curve calculated for the same parameters as curve *2* but under the condition that the X-ray radiation beam falls on a crystal with divergence $\Delta\theta = 4.1 \times 10^{-6}$ rad, which corresponds to experimental detection condition.

We can notice splitting of a peak corresponding to the zero diffraction order in all curves. This splitting is smoothed in curves *1* and *3*, which are obtained and calculated, respectively, in conditions of a divergent incident beam. Despite the fact that all peaks in these curves are almost identical to each other, the background signal in the central part of these curves is substantially different. It is possible that this difference is caused by the additional deformation of the crystal, which is not taken into account in calculations and compresses (additionally focuses) the incident radiation beam. This is because of the known fact that the LiNbO$_3$ crystal, which was grown as a monodomain, is initially in the stressed state. Let us return to the discussion of the peaks.

A collapse in the center of a peak, which corresponds to the zero diffraction order in curve *2*, means that the Bragg reflection disappeared although the radiation incidence angle is as before equal to the Bragg angle for the undeformed crystal lattice. Why did the crystal stopped reflecting? In order to answer this question, let us return to Fig. 10. Let us assume that we gradually increase the SAW amplitude starting from zero. It is evident that SAW slopes will come out from the Bragg reflection conditions at a certain amplitude. However, the regions remain near the SAW maxima and minima for which the Bragg condition is fulfilled as before. As we noted above, the crystal lattice deformation in LiNbO$_3$ has such a character that the crystal is compressed in SAW minima and stretched in maxima. This variation in interplanar distance *d* is precisely the variation that leads to the fact that the regions near SAW maxima and minima are also out of the Bragg reflection conditions. Moreover, since the interplanar distance decreases in SAW minima and increases in maxima, a small variation in the incidence angle into one or another side returns the
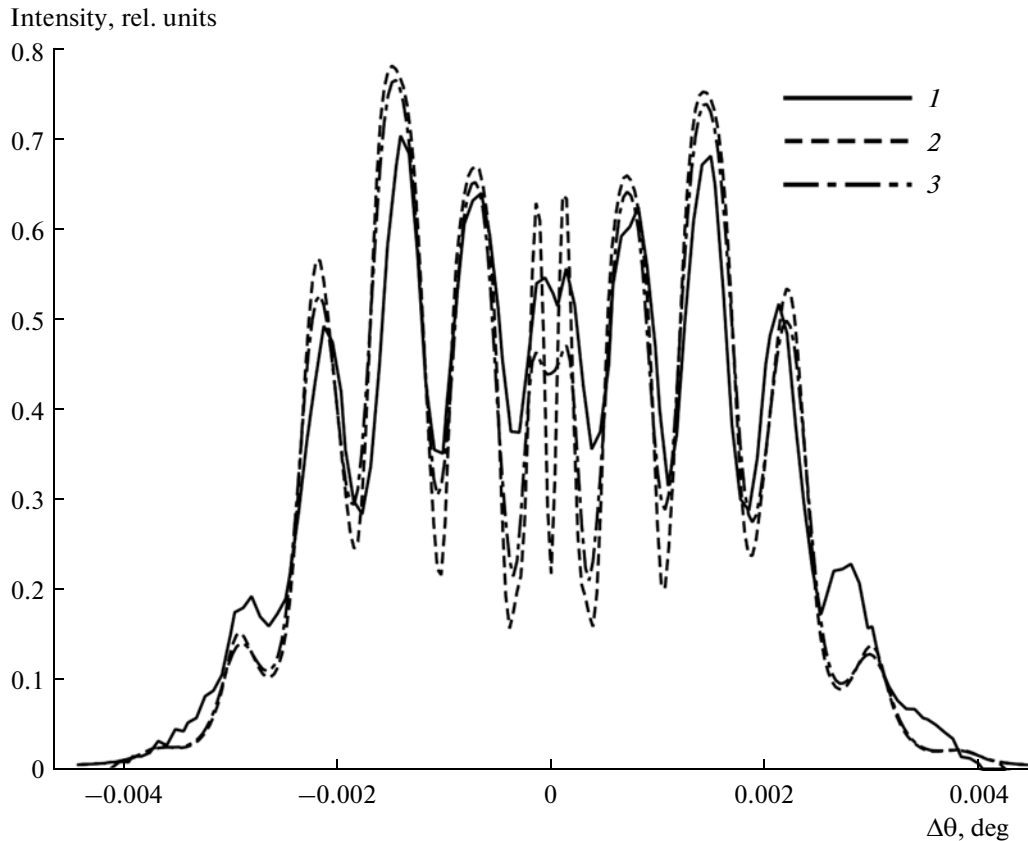
Intensity, rel. units

Fig. 12. Rocking curves from the *YZ* cut of the lithium niobate crystal: (*1*) experimental curve at the signal amplitude across the IDT of 1.2 V (plot axes are to the right and from above); (*2*) the theoretical curve for a plane incident wave at the SAW amplitude of 1/2 of the interplanar spacing; and (*3*) curve *2* for the X-ray radiation beam with divergence $\Delta\theta = 4.1 \times 10^{-6}$ rad.

corresponding regions into the Bragg reflection conditions. We can determine variation Δd of the interplanar distance in SAW maxima and minima by the magnitude $\Delta\theta$ of this splitting:

$$\Delta d = -\frac{d\Delta\theta}{\tan\theta_{Br}}. \qquad (13)$$

In the case under consideration, this quantity was $\Delta d = 1.3 \times 10^{-5}$ Å.

However, this explanation does not exhaust the discussion of splitting of the zero-order peak. The reason is that, as X-ray radiation penetrates into the crystal depth, the SAW-induced crystal lattice deformation damps, and the crystal becomes ideal again. Therefore, the following question, which we should answer, concerns what occurs with the radiation field.

Next, Figs. 13–16 represent the wave-field intensity distributions inside the crystal, which were calculated using (9) for the case of our interest, namely: the incidence angle equals the Bragg angle, $\theta = \theta_{Br}$; SAW amplitude $H = 1/2d$; SAW wavelength $\Lambda = 12$ μm; and the transverse beam size is 100 μm. Figures 13a and 15a represent the field intensity distribution for diffracted wave $|\mathbf{D}_h(\mathbf{r})|^2$, while Figs. 14a and 16a represent

that of the field of transmitted wave $|\mathbf{D}_0(\mathbf{r})|^2$. Fields in Figs. 13 and 14 are calculated without absorption in the crystal and those in Figs. 15 and 16 are calculated with absorption.

Simulated distributions of wave fields show that the radiation indeed cannot penetrate into the crystal depth. However, it also does not emerge on the crystal surface and propagates in the near-surface layer at a depth (the beam axis) of approximately $\Lambda/2$. Moreover, if we assume that absorption is absent in the crystal (Figs. 13, 14), then the beam intensity will continuously increase as the incident radiation is added to the beam. This means that the incident radiation beam is simply redirected in parallel to the crystal surface. In this case, its cross section decreases and, naturally, the beam intensity is proportional to the degree of its compression. In Figs. 13–16, the white beam corresponds to the degree of intensity $2I_0$; blackening in the beam center in Figs. 15 and 16 means that field intensity exceeded this value; and several black-and-white halos in the beam center in Figs. 13 and 14 mean that the field intensity exceeded the normalization value by several times.

In the presence of absorption (Figs. 15, 16), the beam intensity in the crystal comes to a certain fixed value,
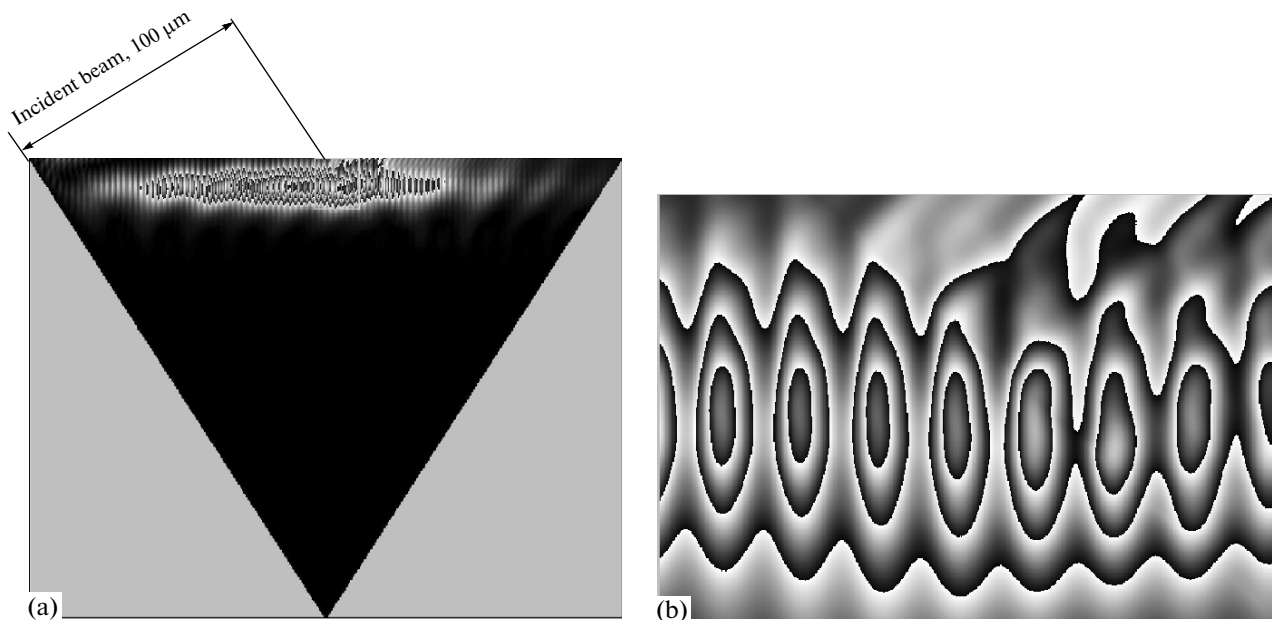
Fig. 13. Field intensity distribution for diffracted wave $|\mathbf{D}_h(\mathbf{r})|^2$ inside the SAW-modulated LiNbO$_3$ crystal (*YZ* cut) without absorption in the case of splitting the zero-order diffraction peak: (a) general view and (b) isolated fragment on the boundary of the incident beam. Fragment sizes correspond to 4Λ along the horizontal and Λ along the vertical.
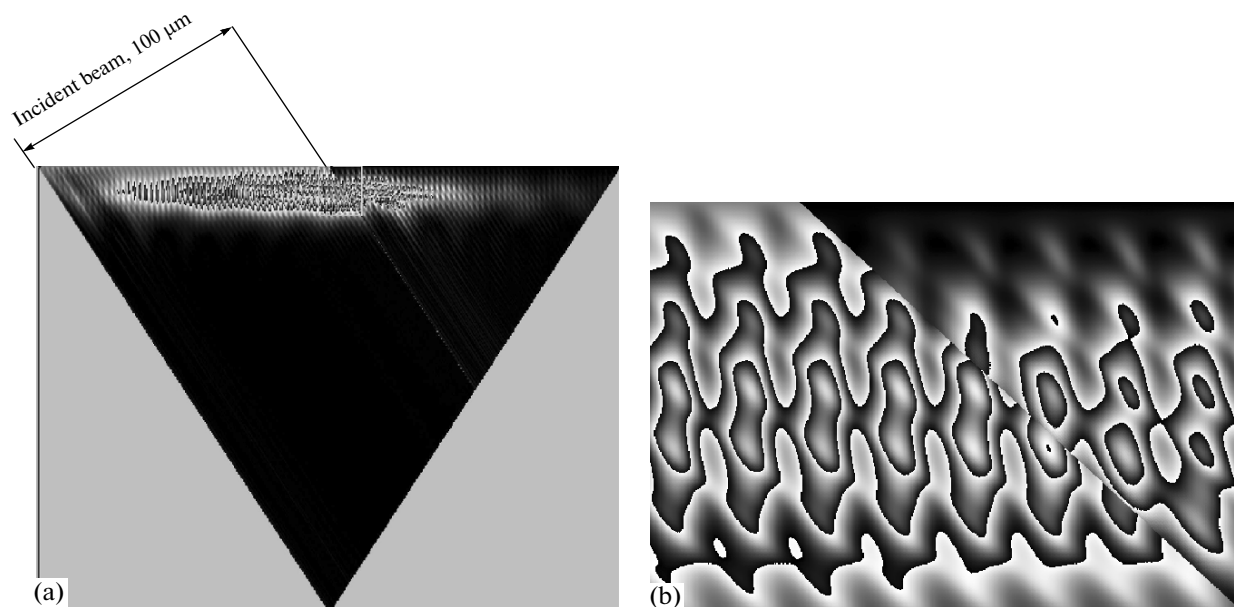

Fig. 14. Field intensity distribution for transmitted wave $|\mathbf{D}_0(\mathbf{r})|^2$ inside the SAW-modulated LiNbO$_3$ crystal (*YZ* cut) without absorption in the case of splitting the zero-order diffraction peak: (a) general view and (b) isolated fragment on the boundary of the incident beam. Fragment sizes correspond to 4Λ along the horizontal and Λ along the vertical.

which is determined by the fact that the beam amplification due to the incident radiation is compensated by its weakening due to the photoelectric absorption.

It is rather simple to understand why radiation cannot penetrate into the crystal depth, but it is difficult to answer the question why it cannot emerge on the crystal surface. The author's interpretation of answering this question that the field of the incident wave that passed strongly deformed near-surface layer eliminates the field of the wave diffracted by a weakly
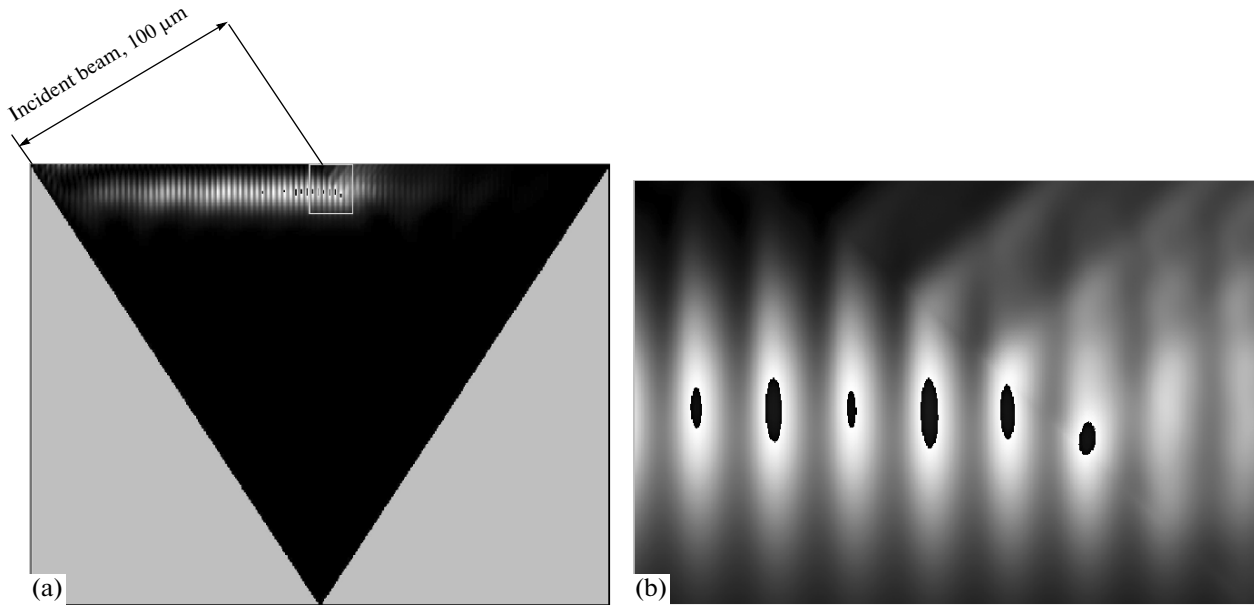
Fig. 15. Field intensity distribution for diffracted wave $|\mathbf{D}_h(\mathbf{r})|^2$ inside the SAW-modulated LiNbO$_3$ crystal (*YZ* cut) with absorption in the case of splitting the zero-order diffraction peak: (a) general view and (b) isolated fragment on the boundary of the incident beam. Fragment sizes correspond to 4Λ along the horizontal and Λ along the vertical.

Fig. 16. Field intensity distribution for transmitted wave $|\mathbf{D}_0(\mathbf{r})|^2$ inside the SAW-modulated LiNbO$_3$ crystal (*YZ* cut) with absorption in the case of splitting the zero-order diffraction peak: (a) general view and (b) isolated fragment on the boundary of the incident beam. Fragment sizes correspond to 4Λ along the horizontal and Λ along the vertical.
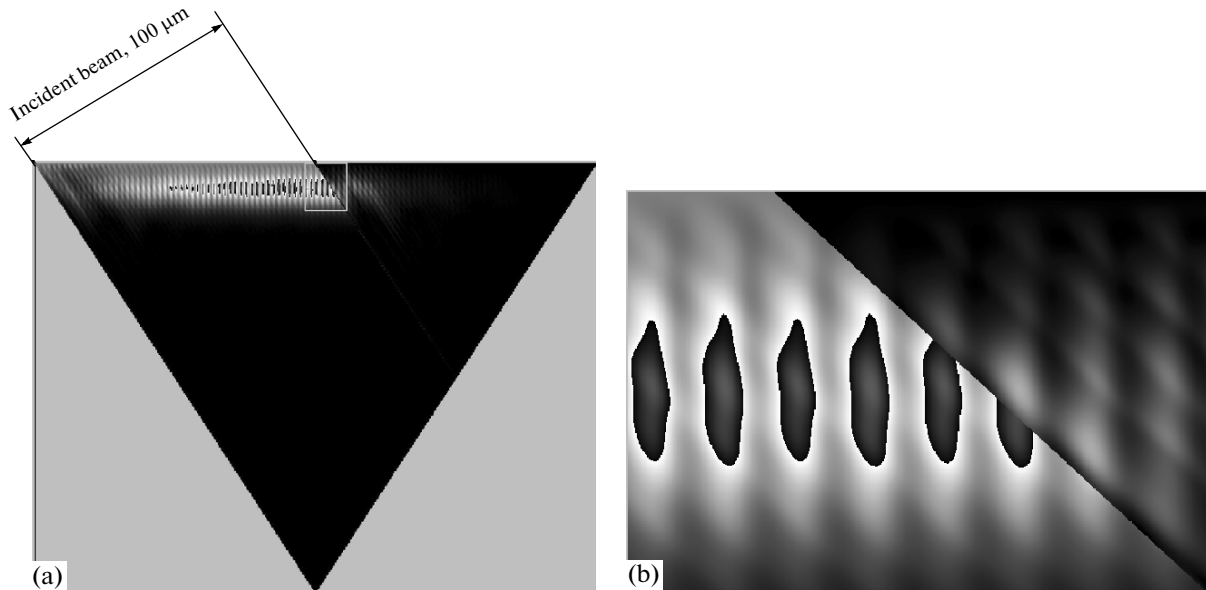
deformed ("ideal") crystal region in the interferential manner not allowing it to emerge on the surface. This is confirmed by intensity distributions of the field of diffracted wave $|\mathbf{D}_h(\mathbf{r})|^2$ (Figs. 13, 15), from which it is seen that the radiation starts to emerge from the crystal immediately as the incident radiation beam is inter-rupted. The radiation emergency region is rather considerable since initially the field energy in the near-surface beam is distributed between waves $\mathbf{D}_h$ and $\mathbf{D}_0$. Figure 14 (the crystal without absorption) shows how field intensity $|\mathbf{D}_0(\mathbf{r})|^2$ slowly drops and, being multiply scattered (Figs. 13, 14), gives energy to wave $\mathbf{D}_h$, which
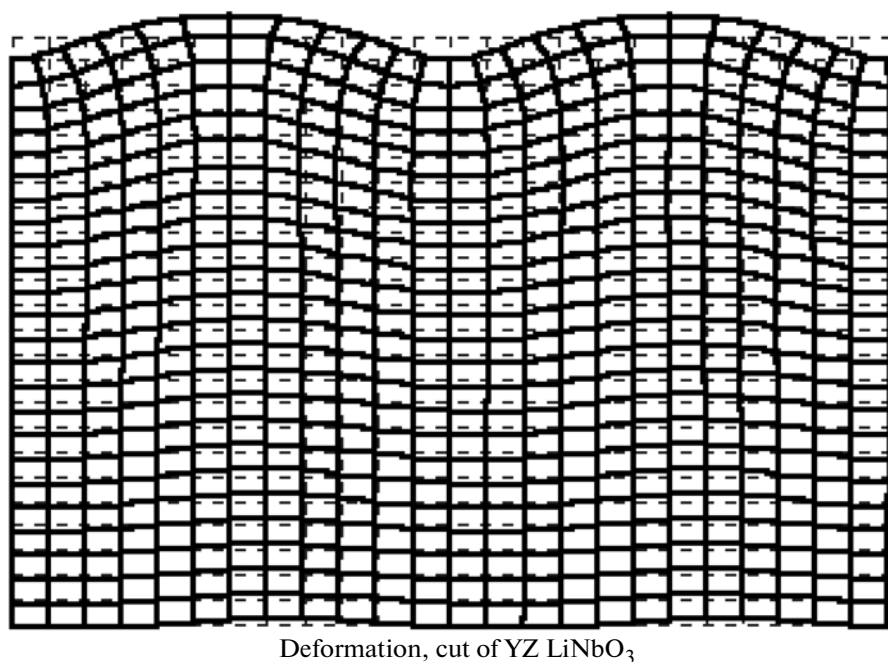
Deformation, cut of YZ LiNbO$_3$

Fig. 17. Deformation of the crystal lattice for the case when the longitudinal shift component in the SAW leaves behind the transverse component by $\pi/2$.

emerges from the crystal. Only due to the photoelectric absorption, because of which the radiation partially remains in the crystal, can we observe splitting of the peaks in the rocking curve.

CONCLUSIONS

It follows from the above that the Bragg diffraction method is a powerful tool for studying the SAW deformation fields. With its help, we can explain such nontrivial effect as splitting of peaks in the rocking curve of the SAW-modulated LiNbO$_3$ crystal. It was possible to reveal this effect only when using the synchrotron radiation beams with the angular divergence of approximately several microradians. The method sensitivity to the crystal lattice deformations is approximately 10^{-5} Å. Because of such sensitivity, the exact calculation of the deformation field is necessary, which is a laborious process even in the case of SAW propagation along the symmetry axis of the crystal.

In order to understand the limitations of the method, we should clearly understand the physical fundamentals of the process. In the case of the Bragg diffraction of X-ray radiation at the *YZ* cut of the lithium niobate crystal, this can be illustrated by the following example. Figure 17 shows the SAW deformation field under the condition of the change in the polarization of the longitudinal component, i.e., now the longitudinal component leaves behind the transverse phase by $\pi/2$, which is erroneous.

If we compare it with the SAW deformation field in Fig. 10, the visual distinction is evident. However, X-ray rocking curves obtained in terms of the discussed method (calculation) for both cases are identical. The reason is that the X-ray radiation, as it penetrates into the crystal depth, propagates, we can say, "by touch," according to the Bragg condition: if it is fulfilled, the radiation is reflected, and if not, it penetrates deeper. This means that rocking curves depend on the average variation in the interplanar distance by the SAW period, which is identical for both cases. Thus, in terms of this method, when quantities proportional to averaged characteristics of the deformation field are detected, the phase difference of SAW components is physically indistinguishable. This is the consequence of the "phase" problem, which is general for optics when the information on the phase of the diffracted radiation turns out lost. To restore it, local investigation methods should be used, for example, topography. However, to obtain the topographic image of the traveling SAW, we should use stroboscopic methods. Another method is the method proposed in [1, 13]. In this method, to obtain the stationary image, the synchronization of the SAW excitation frequency with the rotation period of electron bunches in a synchrotron storage ring is used. For laboratory radiation sources, topography is performed only for stationare SAW fields, such as standing waves [14].

Since the topographic image is the diffraction pattern in the near field, it can also be calculated using the proposed model of the Bragg diffraction. For this pur-

pose, it is sufficient to solve the problem of radiation propagation in free space using the calculated field distribution on the emergency crystal surface. All these facts mean that the problem of X-ray radiation diffraction by the SAW-modulated crystals is solved successfully. The next stage of investigations is planned as the development of the methods for solving the inverse problem: restoration of SAW deformation fields in crystals by the data of X-ray diffraction measurements.

REFERENCES

1. H. Cerva and W. Graeff, Phys. Status Solidi B **82**, 35 (1984).

2. E. Zolotoyabko, D. Shilo, W. Sauer, et al., Rev. Sci. Instrum. **70**, 3341 (1998).

3. E. Zolotoyabko, Nucl. Instrum. Methods Phys. Res. B **147**, 410 (1999).

4. R. Tucoulou, R. Pascal, M. Brunel, et al., J. Appl. Crystallogr. **33**, 1019 (2000).

5. D. V. Roshchupkin and M. Brunel, IEEE Trans. Ultrason., Ferroelectrics, Freq. Control **41**, 512 (1994).

6. D. V. Roshchupkin, I. A. Schelokov, R. Tucoulou, and M. Brunel, IEEE Trans. Ultrason., Ferroelectrics, Freq. Control **42**, 127 (1995).

7. S. Takagi, J. Phys. Soc. Jpn. **26**, 1239 (1969).

8. A. M. Afanas'ev and V. G. Kohn, Acta Crystallogr. A **27**, 421 (1971).

9. A. V. Kolpakov, *Diffraction of X-Rays in Crystals with One-Dimensional Change of Lattice Period* (Mosk. Gos. Univ., Moscow, 1988) [in Russian].

10. E. Dieulesaint and D. Royer, *Ondes Elastique dans les Solides* (Masson, Paris, 1974).

11. A. A. Oliner, *Acoustic Surface Waves* (Springer, Berlin, Heidelberg, New York, 1978).

12. I. A. Schelokov, D. V. Roshchupkin, D. V. Irzhak, and R. Tucoulou, J. Appl. Crystallogr. **37**, 52 (2004).

13. R. W. Whatmore, P. A. Goddard, B. K. Tanner, and G. F. Clark, Nature **299**, 44 (1982).

14. D. V. Irzhak and D. V. Roshchupkin, Poverkhnost', No. 1, 36 (2002).

Translated by N. Korovin